11th International Symposium on Turbulence and Shear Flow Phenomena (TSFP11)
Southampton, UK, July 30 to August 2, 2019

STRUCTURAL ORGANIZATION IN TURBULENT CHANNEL FLOW

Esther Mäteling
Chair of Fluid Mechanics
and Institute of Aerodynamics
RWTH Aachen University
Wüllnerstr. 5a
52062 Aachen, Germany
e.maeteling@aia.rwth-aachen.de

Michael Klaas
Chair of Fluid Mechanics
and Institute of Aerodynamics
RWTH Aachen University
Wüllnerstr. 5a
52062 Aachen, Germany
m.klaas@aia.rwth-aachen.de

Wolfgang Schröder
Chair of Fluid Mechanics
and Institute of Aerodynamics
RWTH Aachen University
Wüllnerstr. 5a
52062 Aachen, Germany
office@aia.rwth-aachen.de

ABSTRACT

The structural organization in a fully developed, turbulent channel flow (TCF) is analyzed experimentally based on two-component velocity and two-dimensional wall-shear stress (WSS) measurements using particle-image velocimetry (PIV) and the micro-pillar shear-stress sensor (MPS^3). The two-dimensional experimental data are used to investigate the influence of large-scale motions (LSM) and very large-scale motions (VLSM) on near-wall small-scale motions (SSM) for five friction Reynolds numbers ranging from $Re_\tau = 375$ to $Re_\tau = 1{,}968$. From the PIV data, LSM and VLSM of the outer layer are identified via uniform momentum zones (UMZ). Their inner composition consists of coherently moving hairpin vortices which are identified by a Galilean decomposition and the swirling strength. The near-wall SSM are detected using the two-dimensional WSS measurements. An Empirical Mode Decomposition (EMD) is applied to subtract large-scale footprints. The wall-normal velocity component at the boundary of the viscous sublayer is calculated based on the WSS data and an EMD yields the large-scale dynamics imposed onto the SSM. Based on these parameters, large-scale and small-scale sweeps and ejections are calculated.
The results show that the number of LSM and VLSM decreases with increasing Reynolds number. Moreover, hairpin vortices appear more frequently and feature a larger size and strength with increasing Reynolds number. While the large scales in the near-wall region show more sweeps than ejections, the SSM feature a reversed situation with more ejections than sweeps. In addition, a small Reynolds number dependence of these events, which does not follow a specific overall trend, is observed.

INTRODUCTION

The important role of turbulent wall-bounded flows in technical systems underlines the necessity to understand the structural organization inside these flows to predict their behavior and to be able to manipulate them to application-specific needs. In recent years, several studies, e.g., Liu et al. (2001) and Balakumar and Adrian (2007), have shown that large-scale flow structures have a major impact on the transport and mixing processes. They influence small-scale near-wall structures by superposition, modulation, and distortions by sweeps and ejections (Agostini and Leschziner (2014, 2016)) via their footprint onto the wall shear-stress distribution (Große and Schröder (2009)). A recent numerical investigation by Cho et al. (2018) showed that, besides the classical energy cascade, two additional interaction processes transfer energy between the small and the large scales. The interaction between larger energy-containing motions is involved in the skin-friction generation, while the transfer from small to large integral scales is related to the formation of the wall-reaching inactive part of the large energy-containing motions.
Following the hairpin vortex packet model introduced by Adrian et al. (2000b), the structural organization in turbulent wall-bounded flows is based on hairpin vortices which tend to travel coherently in packets forming LSM. These motions also tend to concentrate in packets, referred to as VLSM. Jiménez (2012) concluded that each hairpin vortex represents an individual ejection originating at the wall and that ejections also tend to align in streamwise groups which can be linked to packets of hairpin vortices, i.e, LSM, or even to VLSM.
According to Zhou et al. (1999), the heads of hairpin vortices can be detected by the swirling strength. This criterion was successfully applied to turbulent flow fields as a vortex marker by Adrian et al. (2000a). Uniform momentum zones (UMZ), which occur in turbulent confined and

semi-confined flows, are related to the LSM and VLSM. The UMZ were first studied by Meinhart and Adrian (1995) in a boundary layer flow and linked to structural properties of boundary layer flows a few years later by Adrian et al. (2000b). Kwon et al. (2014) applied the technique to turbulent channel flow to investigate the quiescent core but no analysis of the LSM and VLSM in TCF using UMZ can be found in the literature.

A two-dimensional EMD is used to separate the LSM from the SSM. This algorithm splits amplitude- or frequency-modulated signals into a set of Intrinsic Mode Functions (IMF) based on the local characteristic time or space scales. The EMD was originally proposed by Huang et al. (1998) and used by Agostini and Leschziner (2014, 2016) for scale separation of two-dimensional velocity data. By comparing the EMD to other separation algorithms and taking into consideration several studies concerning its efficacy and validity, the authors showed that the EMD is well suited to separate the large from the small scales. Since the energy content of the large scales is comparable to the small-scale energy at high Reynolds numbers, Proper Orthogonal Decomposition will not lead to convincing results. Moreover, no pre-determined functional elements are needed for the EMD like for Fourier or wavelet functions.

In this experimental study, two measurement techniques, namely PIV and the MPS^3, are combined to conduct a detailed analysis of the SSM in the near-wall field and the LSM in the outer flow, which enables a thorough investigation of the modulation cycle as a function of the Reynolds number. To the authors' knowledge the investigation of this modulation based upon the combination of experimentally determined temporally and spatially resolved two-dimensional velocity and WSS data is conducted for TCF for the first time, which opens a new perspective in this field of research. Due to its ability to acquire the two-dimensional wall shear-stress distribution with a high spatial and temporal resolution, the MPS^3 offers the possibility to gain new experimental insights into the dynamics of the small-scale near-wall flow structures. The detection of sweeps and ejections links the near-wall flow field to the outer layer, in which PIV is conducted to analyze the behavior of the governing large-scale structures, i.e., hairpin vortices, LSM, and VLSM, based on the hairpin vortex packet model introduced by Adrian et al. (2000b). The snapshot-based analysis often applied in the literature is expanded by a statistical evaluation of the main features of the SSM and LSM.

EXPERIMENTAL SETUP

The experiments are performed in an Eiffel-type wind tunnel at the Institute of Aerodynamics. A $9{,}000$ *mm* long inlet section with a tripping device at its beginning provides a fully developed, turbulent flow at the $2{,}700$ *mm* long measurement section. The latter features an aspect ratio of $AR = 20$ with a cross-section of 100 x $2{,}000$ mm^2 (height $2h$ x width w) that ensures a negligible influence of three-dimensional effects.

The two-dimensional two-component PIV setup is realized with a *Continuum Minilite* low-speed laser and a *PCO Edge* s-CMOS camera providing a resolution of $2{,}560$ x $2{,}180$ px^2 in combination with a *Zeiss Macro-Planar T* 2/100 ZF.2* lens. The measurement plane is oriented in the streamwise and wall-normal direction at the channel's centerline. The field of view of 100 x 94.5 mm^2 is captured with an optical resolution of 14.2 px/mm. In total, $6{,}000$ image pairs are recorded for each friction Reynolds number in the range of $Re_\tau = \frac{u_\tau h}{\nu} = 375$ to $Re_\tau = 1{,}968$ with an acquisition frequency of 5 Hz. This setup is used for a snapshot-based and statistical analysis of the wall-normal structural organization in the outer layer.

To measure the two-dimensional WSS an MPS^3 mounted onto the channel's sidewall is used. The sensor consists of 9×9 micro-pillars with a height of $L_p = 200$ μm and a diameter of $D_p = 14$ μm. They are arranged in a square with a spacing of $\Delta L_{xy} = 200$ μm leading to a spatial resolution of $\Delta L_{xy}^+ \approx 3.7$ ($Re_\tau = 925$), $\Delta L_{xy}^+ \approx 5.5$ ($Re_\tau = 1{,}419$), and $\Delta L_{xy}^+ \approx 7.6$ ($Re_\tau = 1{,}950$) in viscous scaling. The micro-pillars are illuminated by a high-power LED system in a backlight configuration and their deflection is recorded with a *Photron FASTCAM Mini WX100* high-speed camera in combination with a *K2/SC long-distance microscope* lens yielding an optical resolution of 0.98 $px/\mu m$. At a frequency of $1{,}000$ Hz, $5{,}484$ images are recorded at each Reynolds number. Timestep-based analysis as well as statistics are used to expose the near-wall flow field and to relate the occurring phenomena to the outer LSM.

EVALUATION TECHNIQUES

The flow features derived from the PIV measurements in the streamwise and wall-normal direction are based on the hairpin vortex packet model (Adrian et al. (2000b)). The swirling strength λ_{ci}, which describes the strength of any swirling motion by the imaginary part of the complex eigenvalues of the local velocity gradient tensor, is used to detect the heads of hairpin vortices. The relation is defined as

$$\begin{pmatrix} \frac{\partial u}{\partial x} & \frac{\partial u}{\partial y} \\ \frac{\partial v}{\partial x} & \frac{\partial v}{\partial y} \end{pmatrix} = \begin{bmatrix} v_r & v_{cr} & v_{ci} \end{bmatrix} \begin{bmatrix} \lambda_r & & \\ & \lambda_{cr} & \lambda_{ci} \\ & -\lambda_{ci} & \lambda_{cr} \end{bmatrix} \begin{bmatrix} v_r & v_{cr} & v_{ci} \end{bmatrix}^{-1}, \tag{1}$$

with the real eigenvector v_r, the real eigenvalue λ_r and the pairs of complex conjugated eigenvalues $\lambda_{cr} \pm i\lambda_{ci}$ and eigenvectors $v_{cr} \pm iv_{ci}$. The velocity gradients are obtained using central differences. Areas smaller than 10 % of the largest patch of swirling strength are neglected. In addition, swirling strength values below 1.5 times the rms-value, which is calculated at the most energetic position of the LSM $y^+ = 3.9\sqrt{Re_\tau}$ (Agostini and Leschziner, 2014), are not considered in accordance with Wu and Christensen (2006). Since the LSM and VLSM feature a relatively uniform streamwise velocity magnitude, they are investigated by detecting UMZ. The application of this technique to TCF follows the approach of Adrian et al. (2000b) and Kwon et al. (2014). In general, a histogram of the streamwise velocity component is determined for a single instantaneous velocity field. The associated streamwise velocity magnitude of a local maximum represents the momentum of a possible UMZ and is referred to as *modal velocity*. The outer boundaries of each UMZ are calculated as the mean value between the modal velocities of adjacent UMZ and are characterized by thin regions of large $\frac{\partial u}{\partial y}$. In total, $6{,}000$ snapshots are evaluated and the Reynolds number effect on the mean features, namely number, diameter, and strength of hairpin vortices and number of UMZ, is analyzed.

To show the consistent character of the flow structures apart

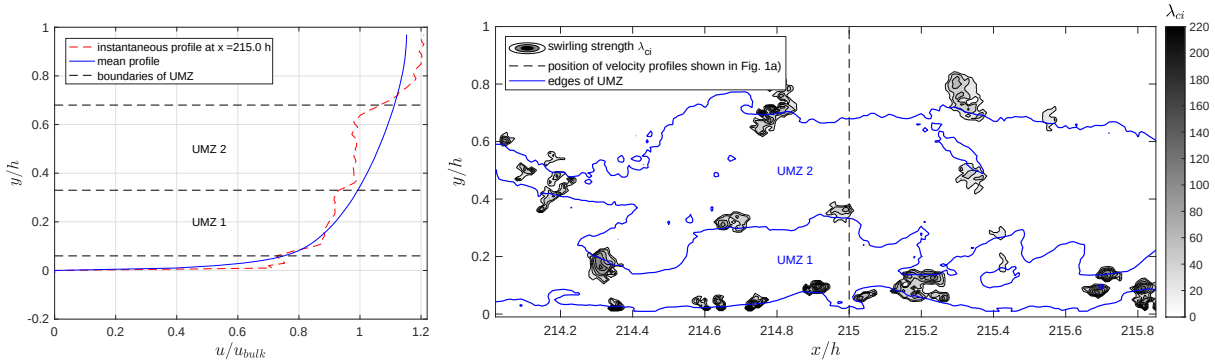

(a) velocity profiles

(b) contour plot with UMZ and swirling strength

Figure 1: Mean and instantaneous velocity profile normalized with the bulk velocity at $x = 215h$ and outer boundaries of UMZ and filled contours of swirling strength λ_{ci} along one channel half at $Re_\tau = 375$.

from the snapshot-based analysis, linear stochastic estimation of the conditionally averaged velocity fluctuation field in the presence of a vortex core, i.e., a hairpin vortex head, is conducted based on the work of Christensen and Adrian (2001). The estimation is given by equation 2 with $u'_j(\mathbf{x}')$ being the velocity fluctuation.

$$\langle u'_j(\mathbf{x}')|\lambda_{ci}(\mathbf{x})\rangle \approx \frac{\langle \lambda_{ci}(\mathbf{x})u'_j(\mathbf{x}')\rangle}{\langle \lambda_{ci}(\mathbf{x})\lambda_{ci}(\mathbf{x})\rangle}\lambda_{ci}(\mathbf{x}) \tag{2}$$

The two-dimensional WSS distribution obtained from the MPS^3 measurements is used to analyze the near-wall flow dynamics. To separate the footprints of the LSM from the SSM, the WSS fluctuations τ' are decomposed by two-dimensional EMD separately for the streamwise and the wall-normal direction. This algorithm produces physically meaningful modal representations from two-dimensional data like amplitude- or frequency-modulated signals by splitting the signal into a set of IMF based on the local characteristic time or space scales. The WSS fluctuations τ' of each snapshot are decomposed into three IMF and a residual, the IMF representing the small scales τ'_{SS} and the residual the large scales τ'_{LS}. Details of the procedure can be found, e.g., in Agostini and Leschziner (2014).
Additionally, the wall-normal velocity component

$$v = -\frac{y^2}{2\eta}\left(\frac{\partial \tau'_x}{\partial x} + \frac{\partial \tau'_z}{\partial z}\right) \tag{3}$$

is calculated based on the continuity equation using the assumption that the velocity profile in the viscous sublayer is linear. The wall-normal position y is calculated with the height of the micro-pillars. The residual obtained by an EMD of the wall-normal velocity fluctuation v' yields the large-scale dynamics v'_{LS}. In combination with the streamwise large-scale WSS fluctuations $\tau'_{x,LS}$, which are proportional to the streamwise velocity at a fixed wall-normal position inside the viscous sublayer, large-scale sweeps ($\tau'_{x,LS} > 0,\ v'_{LS} < 0$) and ejections ($\tau'_{x,LS} < 0,\ v'_{LS} > 0$) can be identified. According to Agostini and Leschziner (2014), these events lead to distortions modulating the SSM. The same procedure is applied to calculate the small-scale sweeps and ejections. Statistical analysis is conducted concerning their mean number and extent depending on the Reynolds number.

RESULTS

The investigation of the organization of the large-scale events in wall-normal direction is based on 6,000 PIV snapshots. The analysis of one single exemplary snapshot is followed by the discussion of the statistical properties as a function of the Reynolds number.
The LSM and VLSM are defined by the occurrence of UMZ. The present field of view in the streamwise direction is smaller than $3h$. Thus, it is not possible to distinguish between LSM and VLSM (Lee et al. (2014)). Hence, for simplicity, only the term LSM is used in the following discussion for all large- and very large-scale motions.
To calculate the UMZ of each snapshot a histogram of the streamwise velocity component of one channel half is determined with 50 bins. Figure 1a depicts a mean and an instantaneous normalized streamwise velocity profile $\frac{u}{u_{bulk}}$ for an arbitrary snapshot at a friction Reynolds number $Re_\tau = 375$ together with the confining contours of the UMZ, which demonstrates the relatively uniform velocity magnitude inside each UMZ. To analyze the synergy of hairpin vortices and LSM, the entire field of view in the streamwise direction from one channel wall to the centerline is pictured in figure 1b. The confining contours of the UMZ are overlaid by filled contours of swirling strength λ_{ci} representing the heads of hairpin vortices. The validity of the latter is proved by a Galilean decomposition of the velocity field based on the vortex definition of Kline and Robinson (1990) and Robinson (1990). It states that streamlines arrange circular at a vortex core, i.e., a hairpin vortex head, if the convection velocity of this particular vortex is subtracted from the instantaneous field. Hence, various convection velocities are subtracted to visualize all vortex cores and their excellent match with patches of swirling strength reveal the validity of this less time-consuming technique. Due to a lack of space, the results are not shown here.
Figure 1b shows that, with a few exceptions, the heads of hairpin vortices are located on the boundaries of the UMZ. Hence, the heads can be interpreted to act as an upper boundary of each LSM, while the remaining part of the hairpin vortices is encompassed by the LSM. This implies that all hairpin vortices inside one LSM travel with a uniform streamwise momentum. However, a few hairpin vortex heads do not collapse with an outer contour of a UMZ, e.g., the head at $(\frac{x}{h};\frac{y}{h}) = (215.7;0.1)$. These structures build small and young patches that exist within

the larger packets detected by the UMZ algorithm. These findings coincide with the conclusions made by Adrian et al. (2000b).

To show the consistent character of the hairpin vortices besides the snapshot-based analysis, figure 2 exemplarily presents the linear stochastic estimation of the conditionally averaged velocity fluctuation field in the presence of a vortex core, i.e, a hairpin vortex head, at a Reynolds number $Re_\tau = 941$. In total, $6,000$ snapshots are used for the calculation and for clarity, only every second velocity vector is plotted. The length of the vectors is normalized by the local magnitude of the velocity fluctuation since the velocity field is strongest around the event location and weaker features would appear less distinct. The position and peak value of the most intense swirling strength patch of an arbitrary snapshot are used as the event location. Contours of the swirling strength of this snapshot are overlaid in figure 2, and the event location is marked with a solid circle. A distinct swirling motion is visible at the event location in combination with an ejection upstream and below as it is typically observed when a Galilean decomposition is applied to an instantaneous velocity field. Additional swirling patterns labeled $A-E$ appear downstream of the event and are aligned in a line which is inclined from the wall. The motions are slightly blurred in streamwise direction due to the fluctuation of the mean vortex spacing from hairpin vortex packet to packet. This becomes also apparent when comparing the locations of the averaged swirling motions to the patches of swirling strength from the single snapshot. Nevertheless, the spiral patterns visible in the estimated velocity field show how dominant, persistent, and well-organized the hairpin vortices behave inside the TCF.

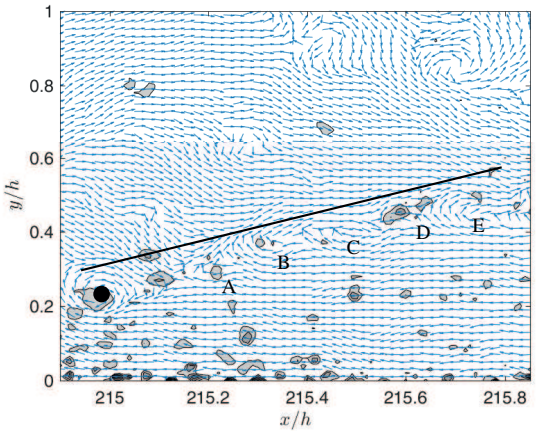

Figure 2: Conditionally averaged velocity fluctuation field in the presence of a vortex core (solid circle) at $Re_\tau = 941$ based on $6,000$ snapshots.

A statistical evaluation of the flow structures which are present in the $6,000$ recorded PIV snapshots is summarized in figure 3 and table 1 for five Reynolds numbers between $Re_\tau = 375$ and $Re_\tau = 1,968$. Figure 3 shows the mean number, the mean diameter, and the mean strength of the hairpin vortex heads normalized by the corresponding values at the lowest Reynolds number $Re_\tau = 375$ as a function of the Reynolds number. While the mean number

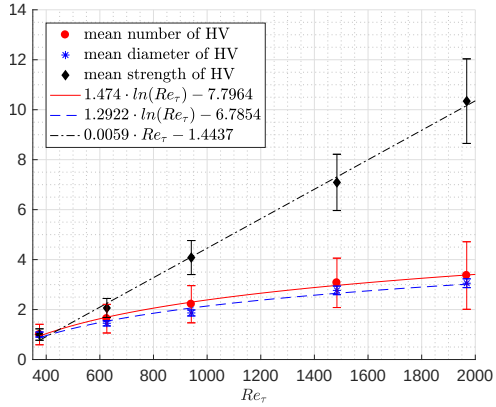

Figure 3: Mean features of hairpin vortex heads (HV) in $6,000$ snapshots at different Reynolds numbers normalized by the corresponding mean value at $Re_\tau = 375$.

and diameter of the hairpin vortex heads follow a logarithmic increase with increasing Reynolds number, the mean strength of the hairpin vortex heads grows linearly. As shown by the values in table 1, the mean number of LSM decreases at higher Reynolds numbers. As a consequence, a higher number of hairpin vortices is incorporated into one LSM, which was also observed by Christensen and Adrian (2001) when comparing the structural behavior at $Re_\tau = 547$ and $Re_\tau = 1,734$ in TCF.

Table 1: Mean number of LSM in $6,000$ snapshots at different Reynolds numbers.

Re_τ	375	626	941	1,484	1,968
LSM	2.02	1.96	1.95	1.59	1.40

In the following, the investigation of the near-wall small-scale dynamics and their synergy with the outer large-scale events is presented. This analysis includes exemplary snapshot-based results as well as a statistical analysis.

Table 2 shows the mean WSS obtained by the MPS^3 measurements based on $5,484$ snapshots for three Reynolds numbers. The values fit very well to the theoretical values of a fully developed TCF, which are additionally listed for comparison.

Table 2: Experimentally obtained and theoretical mean WSS in $[Pa]$ at different Reynolds numbers.

Re_τ	925	1,419	1,950
τ_w (MPS^3)	0.0992	0.2173	0.4126
τ_w (theor.)	0.0985	0.2307	0.4347

Exemplarily, figure 4 shows the total (figure 4a), the large-scale (figure 4b), and the small-scale (figure 4c) WSS fluctuations of an arbitrary snapshot at $Re_\tau = 925$, which are separated by EMD. The color contours represent the corresponding fluctuation in the streamwise direction and the vectors show the fluctuation in both directions. A comparison of the figures reveals that only the magnitude of the small scales is affected by the large-scale fluctuations

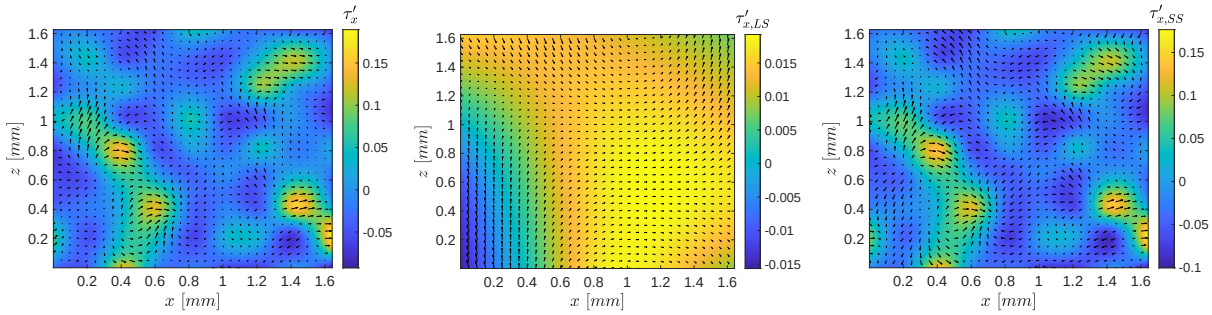

(a) WSS fluctuations τ' (b) large-scale WSS fluctuations τ'_{LS} (c) small-scale WSS fluctuations τ'_{SS}

Figure 4: Total, large-scale, and small-scale WSS fluctuations of an arbitrary snapshot at $Re_\tau = 925$.

but their character, i.e, their shape and extension, is maintained.

To link the small-scale dynamics to the structures of the outer layer captured by the PIV data, sweeps and ejections are detected. Therefore, the orientation of the large-scale wall-normal velocity fluctuation v'_{LS} and the sign of the local large-scale streamwise WSS fluctuation $\tau'_{x,LS}$ are used to identify large-scale sweeps ($\tau'_{x,LS} > 0$, $v'_{LS} < 0$) and ejections ($\tau'_{x,LS} < 0$, $v'_{LS} > 0$). Analogously, the small-scale sweeps and ejections are identified using the small-scale components $\tau'_{x,SS}$ and v'_{SS}. Figure 5 exemplarily visualizes a result of this procedure for the snapshot pictured in figure 4. The total (figure 5a), the large-scale (figure 5b), and the small-scale (figure 5c) wall-normal velocity components are displayed via color contours and the vectors represent the WSS fluctuations, which are also scale separated. As for the WSS fluctuations, the large-scale velocity only influences the magnitude of the SSM.

Table 3: Mean number (#) of large-scale (LS) and small-scale (SS) ejections and sweeps in 37 snapshots at different Reynolds numbers.

Re_τ	925	1,419	1,950
# LS ejections	2.77	2.56	2.11
# LS sweeps	3.22	3.49	3.17
# SS ejections	18.69	20.74	20.06
# SS sweeps	11.69	13.31	14.31

Table 3 summarizes the mean number of large-scale and small-scale sweeps and ejections averaged over 37 snapshots for three Reynolds numbers. In general, more large-scale sweeps than ejections are detected for each Reynolds number, which might be the reason of the asymmetric small-scale modulation described by Agostini and Leschziner (2014). Additionally, the large-scale sweeps nearly occupy one quarter of each snapshot, while the ejections only cover about 10 %.

An increasing Reynolds number leads to a decrease of the number of large-scale ejections. However, there is no clear trend for the large-scale sweeps. An increase from $Re_\tau = 925$ to $Re_\tau = 1,419$ leads to a minor increase of the mean number of large-scale sweeps, but their number decreases again when the Reynolds number increases to $Re_\tau = 1,950$.

In contrast to the large-scales, more ejections than sweeps are detected at the small scales. The same observation was made by Agostini and Leschziner (2014) in 60 snapshots at $Re_\tau = 1,025$. The number of small-scale sweeps gradually increases with increasing Reynolds number.

According to Jiménez (2012), instabilities of the shear layers around streaks created by ejections could cause the evolution of hairpin vortices. Since ejections tend to align in streamwise groups, they can possibly be linked to packets of hairpin vortices, i.e., LSM and VLSM (Jiménez (2012)). Thus, it is an obvious assumption to expect an increasing number of small-scale ejections with increasing Reynolds number because of the higher amount of hairpin vortices (see figure 3). Based on the three Reynolds numbers considered in the present study, this assumption is only partly confirmed by the evolution of the averaged amount of small-scale ejections shown in table 3. From $Re_\tau = 925$ to $Re_\tau = 1,419$, more ejections are detected but their number is reduced for $Re_\tau = 1,950$. Since the MPS^3 field of view in streamwise direction is more than 60 times smaller than the PIV measurement plane and the experimental setup does not allow for time-resolved data which could extend the spatial domain based on Taylor's hypothesis, a direct comparison between the amount of ejections and hairpin vortices is not possible, and further studies need to be performed to understand the synergy of hairpin vortices and ejections.

SUMMARY AND OUTLOOK

The experimental study investigates the structural organization inside a TCF at five friction Reynolds numbers between $Re_\tau = 375$ and $Re_\tau = 1,968$. The two-dimensional velocity distribution in the streamwise and wall-normal direction is obtained from PIV measurements and used to analyze the behavior of outer large-scale events, namely hairpin vortices, LSM, and VLSM. An MPS^3 provides two-dimensional, time-resolved WSS data which reveals the dynamics of the near-wall SSM.

While the hairpin vortex heads are detected by the swirling strength, LSM and VLSM are related to UMZ. It is shown that, in most cases, the hairpin vortex heads are located on the confining boundaries of the UMZ. Thus, they seem to define the upper edge of each (V)LSM while the legs of the hairpin vortices are encompassed by the (V)LSM. A statistical analysis based on 6,000 snapshots reveals that the mean number and diameter of the hairpin vortex heads, normalized by the value at the lowest Reynolds number, follow a

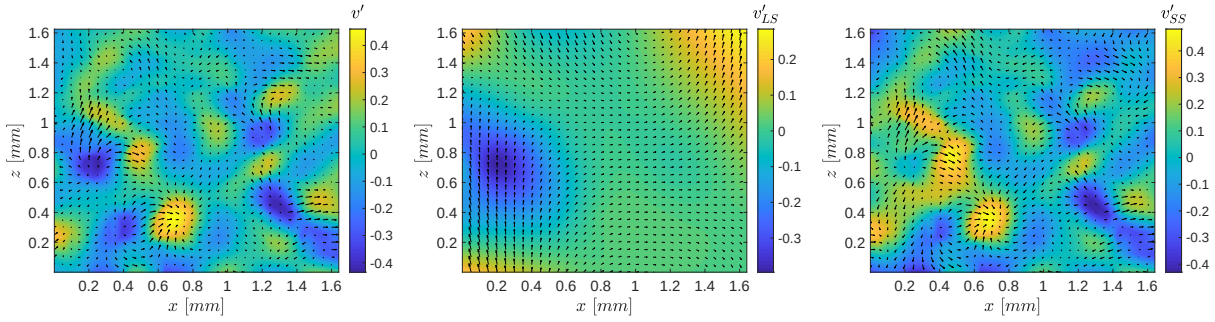

(a) v-component v' (b) large-scale v-component v'_{LS} (c) small-scale v-component v'_{SS}

Figure 5: Total, large-scale, and small-scale wall-normal velocity component (contours) and corresponding WSS fluctuations (vectors) of the same snapshot shown in figure 4.

logarithmic increase with increasing Reynolds number. The mean strength, also normalized, increases linearly. Contrarily, the mean number of LSM decreases with increasing Reynolds number, which results in more hairpin vortices incorporated into each LSM.

The two-dimensional WSS distribution is used to calculate the wall-normal velocity component at the edge of the viscous sublayer. By applying an EMD, the large-scale wall-normal velocity fluctuations are separated from the small-scale fluctuations. The same algorithm is used to subtract the footprint of the LSM from the WSS fluctuations. The analysis of 37 snapshots reveals more large-scale sweeps with a greater extent than large-scale ejections, which might cause the asymmetric small-scale modulation. The small-scales show an opposite behavior.

The findings of this study mostly rely on statistical analysis separately performed for the large-scale events and the small-scale dynamics, which is adequate for investigating the Reynolds number effects. Nevertheless, to deepen the knowledge about their interactions, spatially and temporally resolved, simultaneous data are needed. Thus, in the future, simultaneous PIV and MPS^3 measurements have to be conducted. In addition, the MPS^3 area needs to be enlarged to capture a wider field of view such that the use of Taylor's hypothesis can be avoided.

REFERENCES

Adrian, R., Christensen, K., & Liu, Z.-C. 2000a. Analysis and interpretation of instantaneous turbulent velocity fields. *Experiments in Fluids*, 29(3):275–290.

Adrian, R. J., Meinhart, C. D., & Tomkins, C. D. 2000b. Vortex organization in the outer region of the turbulent boundary layer. *Journal of Fluid Mechanics*, 422:1–54.

Agostini, L. & Leschziner, M. 2014. On the influence of outer large-scale structures on near-wall turbulence in channel flow. *Physics of Fluids*, 26(7):075107.

Agostini, L. & Leschziner, M. 2016. On the validity of the quasi-steady-turbulence hypothesis in representing the effects of large scales on small scales in boundary layers. *Physics of Fluids*, 28(4):045102.

Balakumar, B. & Adrian, R. 2007. Large- and very-large-scale motions in channel and boundary-layer flows. *Philosophical Transactions of the Royal Society of London A: Mathematical, Physical and Engineering Sciences*, 365(1852):665–681.

Cho, M., Hwang, Y., & Choi, H. 2018. Scale interactions and spectral energy transfer in turbulent channel flow. *Journal of Fluid Mechanics*, 854:474–504.

Christensen, K. & Adrian, R. J. 2001. Statistical evidence of hairpin vortex packets in wall turbulence. *Journal of Fluid Mechanics*, 431:433–443.

Große, S. & Schröder, W. 2009. Wall-shear stress patterns of coherent structures in turbulent duct flow. *Journal of Fluid Mechanics*, 633:147–158.

Huang, N. E., Shen, Z., Long, S. R., Wu, M. C., Shih, H. H., Zheng, Q., Yen, N.-C., Tung, C. C., & Liu, H. H. 1998. The empirical mode decomposition and the hilbert spectrum for nonlinear and non-stationary time series analysis. *Proceedings of the Royal Society of London. Series A: Mathematical, Physical and Engineering Sciences*, 454(1971):903–995.

Jiménez, J. 2012. Cascades in wall-bounded turbulence. *Annual Review of Fluid Mechanics*, 44:27–45.

Kline, S. & Robinson, S. 1990. Quasi-coherent structures in the turbulent boundary layer. Part I: Status report on a community-wide summary of the data. *Near-wall turbulence*, pages 200–217.

Kwon, Y., Philip, J., de Silva, C., Hutchins, N., & Monty, J. 2014. The quiescent core of turbulent channel flow. *Journal of Fluid Mechanics*, 751:228–254.

Lee, J., Lee, J. H., Choi, J.-I., & Sung, H. J. 2014. Spatial organization of large-and very-large-scale motions in a turbulent channel flow. *Journal of Fluid Mechanics*, 749:818–840.

Liu, Z., Adrian, R., & Hanratty, T. 2001. Large-scale modes of turbulent channel flow: Transport and structure. *Journal of Fluid Mechanics*, 448:53–80.

Meinhart, C. D. & Adrian, R. J. 1995. On the existence of uniform momentum zones in a turbulent boundary layer. *Physics of Fluids*, 7(4):694–696.

Robinson, S. 1990. Quasi-coherent structures in the turbulent boundary layer. Part II: Verification and new information from a numerically simulated flat-plate boundary layer. In *Near-Wall Turbulence: 1988 Zoran Zaric Memorial Conference Hemisphere, New York*, pages 218–247.

Wu, Y. & Christensen, K. T. 2006. Population trends of spanwise vortices in wall turbulence. *Journal of Fluid Mechanics*, 568:55–76.

Zhou, J., Adrian, R. J., Balachandar, S., & Kendall, T. 1999. Mechanisms for generating coherent packets of hairpin vortices in channel flow. *Journal of Fluid Mechanics*, 387:353–396.